Corresponding author:
Jon Ander Esnaola
jaesnaola@mondragon.edu
cell:+34 635 739 144

Fatigue life estimation of cast aluminium alloys considering the effect of porosity on initiation and propagation phases.

R. Hidalgo[a,b], J. A. Esnaola[a], I. Llavori[a], M. Larrañaga[a], I. Hurtado[b], N. Herrero-Dorca[b]

[a] Structural Mechanics and Design, Engineering Faculty, Mondragon Unibertsitatea, Mondragon, Spain

[b] Advanced Material Forming Processes, Engineering Faculty, Mondragon Unibertsitatea, Mondragon, Spain

ABSTRACT

Porosity is one of the main parameters in the fatigue life of cast alloys as it affects both crack initiation and propagation phases. However, most fatigue assessments present a lack of accuracy as they only consider the effect of the initial pore on the fatigue limit. Therefore, in the present study, first, the effect of the main porosity characteristics on the crack initiation and propagation phases is evaluated. Then, an alternative fatigue assessment model is proposed and implemented for Low Pressure Die Casting (LPDC) A356-T6 aluminium alloy. The model accounts for the effect of the initial pore size and distance to surface on the initiation phase as well as fractographic porosity and average pore size on the fracture surface on the propagation phase. Finally, the model was validated by means of experimental tests. Results have shown that the proposed model is able to qualitatively predict the scatter trend of samples tested at the same load. In addition, the model presents high quantitative accuracy in life estimation with an average logarithmic error below 2% and an absolute average error below 16%.

Keywords: cast aluminium alloys, casting defects, porosity, fatigue life.

NOMENCLATURE

AFD	Average pore Feret Diameter on the fracture surface (mm)
$C(N_b)$	Propagation cycles correction function
d_H	Horizontal distance to crack tip (mm)
DT	Destructive Testing
d_V	Vertical distance from the initial pore to the surface (mm)
f_p	Fractographic average porosity (%)
i (subscript)	Represents each evaluated case
K_{max}	Maximum stress intensity factor (MPa√mm)
LPDC	Low-Pressure Die Casting
LSM	Level Set Method
N_b	Number of cycles calculated with Basquin equation
NDT	Non-Destructive Testing
N_{exp}	Experimental number of cycles corresponding to the failure of the specimen
N_i	Number of cycles corresponding to the initiation phase
N_p	Number of cycles corresponding to the propagation phase
N_t	Predicted total fatigue life
p_r	Propagation speed ratio
S_a	Stress amplitude (MPa)
SIF	Stress Intensity Factor
α	Initiation to total life ratio
φ	Feret Diameter of the initial pore (mm)

1 INTRODUCTION

Casting aluminium alloys are widely employed in the automotive industry due to their high strength-to-weight ratio. Particularly, structural components such as knuckles, suspension components or brake callipers, among others, are subjected to severe cyclical loads and, consequently, they can undergo fatigue problems. Fatigue phenomena is characterised by a high life scatter related to many factors such as notches, stress concentrators, surface quality or residual stresses [1]. In casting components, this scatter is even more notorious owing to microstructural inhomogeneities and defects such as porosity or inclusions [2]. Thus, Low-Pressure Die Casting (LPDC) is especially suitable for manufacturing this type of component as it provides lower porosity and defects than other casting techniques [3].

Several studies have demonstrated that, in the presence of defects, the effect of microstructural aspects such as SDAS, grain size or eutectic particles in the fatigue behaviour can be neglected [4,5]. The main defects that affect the fatigue life of casting components are porosity and inclusions. Between them, many authors have reported porosity as the most detrimental parameter [6–9].

A large number of studies can be found in the literature focused on the influence of porosity in the fatigue life of casting components. Most of the works analyse the influence of surface or near surface pores in the crack initiation stage and their influence on the total fatigue life [4,8,10–14]. The pores reduce the time to crack initiation by creating a high-stress concentration region adjacent to this microstructural defect [10]. As a result, many authors have proposed fatigue limit estimation procedures dependent on different parameters of the initial pore. The Linear Elastic Fracture Mechanics (LEFM) approach was one of the most widely used techniques [6,15]. Alternative works, such as that conducted by Murakami *et al.* [16], estimated the fatigue limit considering the $\sqrt{area}$ parameter related to the defect size. Other works such as the Theory of Critical Distances (TCD) proposed by Susmel and Taylor [17] and the Gradient Criterion (GR) proposed by Nadot [18], considered the stress field around a defect to predict the fatigue life of the component under study. Nevertheless, all these methods only take into account the effect of the initial pore on the fatigue limit.

In contrast, some authors have pointed out that not only the initial pore has an effect on the fatigue behaviour of casting Al alloys but also the overall microporosity present in the samples, which has an effect on the propagation phase [7,19–21]. Thus, H. R. Ammar *et al.* [12] demonstrated that the high-stress concentration associated with large pores (gas pores) increases the crack propagation rate compared to the effect of small multiple pores (shrinkage porosity) for similar average porosity values, thereby decreasing fatigue life. In addition, higher microporosity level also increases the crack propagation rate [19].

However, few fatigue life estimation approaches in the literature consider the influence of microporosity on the crack propagation. Choong Do Lee *et al.* [7] proposed a modification of Basquin's equation to include the effect of microporosity on fatigue life prediction. However, the proposed procedure still presents a lack of accuracy.

In conclusion, the different approaches found in the literature still lack precision when it comes to fatigue life estimation of cast components as they do not consider the effect of porosity in both initiation and propagation phases. With a view to tackling such limitations, the present work proposes an alternative fatigue model that considers the effect of porosity in both the initiation and propagation phases.

2 THEORETICAL PROCEDURE

In most of the fatigue assessment models, for example the Basquin equation, which proposes a linear relationship in log-log scale between the stress amplitude and fatigue lifetime, a simple linear regression allows the definition of the stress-fatigue lifetime field (*S*-*N*). However, fatigue specimens or components do not show repetitive behaviour when tested at the same load condition due to many factors such as defects or surface finish and, therefore, a scatter in fatigue life is found. The effect of such factors is generally considered by means of coefficients that transform the load/life curve into a scatter band, or probabilistic approaches that provide the probability of failure of a specimen at a certain number of cycles [22].

Particularly, porosity was reported as the main affecting defect in the fatigue life for casting components [6–8]. As an alternative, the proposed procedure intends to capture the effect of porosity found in the tested specimens or components in both initiation and propagation phases, to estimate the fatigue life and minimize the problem of scattering. The proposed procedure is limited to HCF regime and was developed for A356-T6 aluminium alloy obtained by LPDC. The procedure consists of the following steps:

1. **Material S-N curve characterisation:** In common with most HCF assessment methods, the proposed procedure requires characterisation of the S-N curve of the material as a starting point. Furthermore, fracture surfaces have to be analysed to obtain the fractographic average porosity (f_p) and the average size of pores represented by the Average Feret Diameter (*AFD*).
2. **Propagation model considering porosity:** After this, a propagation analytical model that considers the effect of f_p and the *AFD* of the evaluated specimen/component on the propagation speed is applied. The variation of the propagation speed with respect to the material data case is directly related to the propagation cycles. Thus, the propagation number of cycles N_p can be estimated. The propagation model was obtained through a numerical crack propagation sensitivity study for a determined f_p and *AFD* range according to typical LPDC components data.
3. **Initiation model considering initial pore:** Once the propagation cycles have been determined, initiation cycles N_i are estimated according to an analytical model that considers the effect of the initiation pore size and the distance to surface in each evaluated case. The initiation model is based on the maximum stress intensity factor K_{max} and the cycle regime. As a result, the same stress intensity factor has a different effect on the initiation phase depending on whether the evaluated case is in the lower or the higher domain of the HCF regime. The maximum stress intensity factor K_{max} is given by an analytical equation obtained through a numerical sensitivity analysis that considers the initial pore size and the distance to the surface. The sensitivity analysis range was set for typical data values corresponding to LPDC components. The cycle domain inside the HCF regime is provided by Basquin total life N_b according to the initial S-N curve.
4. **Total life estimation:** Once propagation cycles N_p and initiation cycles N_i are estimated, the model provides the total life prediction for each evaluated case.

Fig. 1 represents the flow chart to implement the proposed model for a determined material.

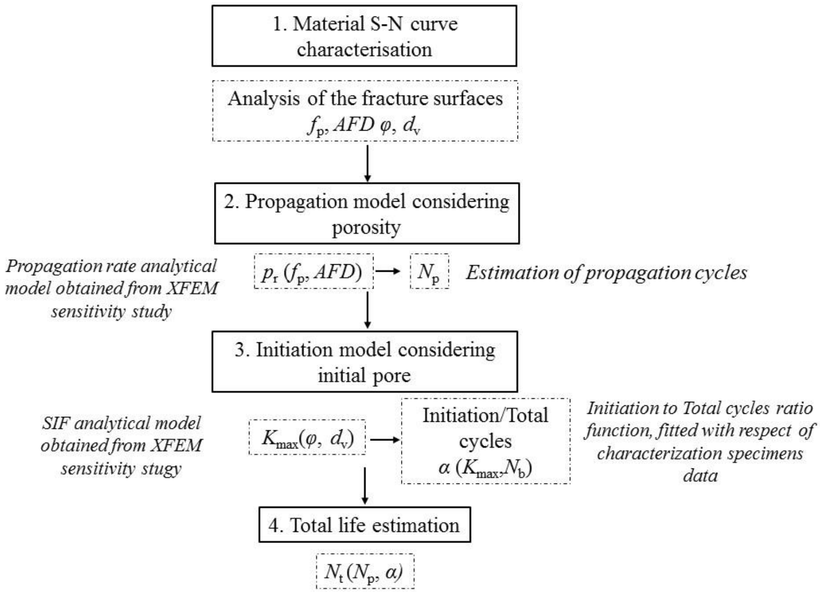

Fig. 1 Flow chart to implement the proposed model of a determined material

The procedure was implemented to evaluate the fatigue life of specimens obtained from LPDC components and experimentally validated.

2.1 Propagation model considering porosity

As was explained in the introduction, porosity has a negative effect on the crack propagation phase. Thus, higher porosity level implies a higher propagation rate and lower propagation number of cycles to final failure [19]. Moreover, for the same porosity level, the propagation rate varies depending on the pore size [12]. For this reason, the present model considers both the effect of porosity f_p and the average pore size *AFD* on the crack propagation speed.

To obtain the propagation model, firstly, specimens used in the initial S-N curve characterisation where the crack initiation pore was located in the surface were identified. It was assumed that, in those cases, the crack initiation cycles are negligible and total life N_t and propagation life N_p can be considered the same. Thus, those cases were considered as reference cases and the propagation rate was normalized for their average f_p and *AFD* values.

Then, XFEM crack propagation simulations were performed for a specified f_p and *AFD* range according to typical LPDC components data (f_p range from 0.5-4% and *AFD* range from 0.1-0.3 mm). Thus, the response surface of the propagation speed with respect to the reference cases ratio p_r was obtained. Fig. 3 shows the XFEM 2D plane strain model domain of 14x7 mm^2. Pores were modelled as perfect equidistant circles of diameter equal to the *AFD* value of each simulated case and f_p was related to the number of pores for the defined domain cross-section.

A general mesh size of 0.5 mm and local mesh size of 0.03 mm near the pores was employed. The Paris coefficients $C=9.11\cdot10^{-8}$ m/cycle/(MPa·√m)^m and $m=0.9981$ corresponding to an A356 Sr modified alloy solutionized at 540 ºC for 1.5 h and artificially aged at 155 ºC for 12 h were used [23]. The crack propagation architecture used was the one presented by Llavori et al. [24]. The XFEM model methodology is explained in Fig. 2. Firstly, the input file with the geometrical model is generated. Secondly, the crack segment is defined and, through the Level Set Method (LSM), the nodes intersected by the crack are identified. Then, the XFEM simulation is performed and the Stress Intensity Factor (SIF) is computed through the interaction integrals and the crack propagation rate is calculated. This procedure is repeated until the failure criteria is fulfilled ($\Delta K \geq \Delta K_c$).

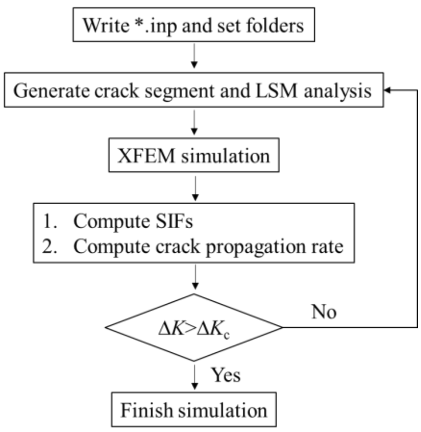

Fig. 2. Flowchart showing the computational sequence of the XFEM analysis developed in [25].

As a result of the XFEM simulations, the propagation speed ratio response surface $p_r(f_p,AFD)$ with respect to the reference p_r=1 case was obtained. Table 1 shows the simulated f_p and *AFD* cases.

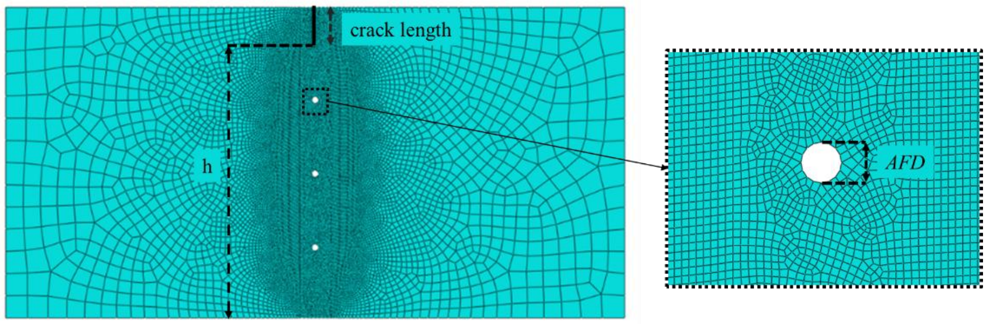

Fig. 3. Details of the XFEM propagation model.

Table 1. f_p and AFD cases considered to obtain the pr(f_p,AFD) surface response

f_p (%)	0.5	1.5	3	4	-
***AFD* (mm)**	0.1	0.15	0.2	0.25	0.3

Once $p_r(f_p,AFD)$ was obtained, the propagation number of cycles N_p was estimated. To this end, a correction function $C(N_b)$ that correlates the Basquin total life prediction N_b (1) with the corresponding N_p was used together with $p_r(f_p, AFD)$ (2).

$$N_b = \left(\frac{S_a}{\sigma'_f}\right)^{\frac{1}{b}} \tag{1}$$

$$N_p\left(f_p, AFD\right) = N_b \frac{C(N_b)}{p_r(f_p, AFD)} \tag{2}$$

The correction function $C(N_b)$ was obtained by applying the best fit technique to the corresponding $C(N_{b\_i})$ values of each reference specimen where the initiation phase was negligible. Additionally, each specimen's propagation speed ratio $p_{r\_i}(f_p,AFD)$ was considered. Hence, the total life $N_{exp\_ref\_i}$ of each reference case can be considered equal to the propagation cycles $N_{p\_ref\_i}$ and correlated with each Basquin total life prediction N_{b_i} with the corresponding $C(N_{b\_i})$ value (3), (4).

$$N_{exp\_ref\_i} = N_{p\_ref\_i} = N_{b\_i} \frac{C(N_{b\_i})}{p_{r\_i}(f_{p,} AFD)} \tag{3}$$

$$C(N_{\mathrm{b}\_i}) = \frac{N_{\mathrm{t\_ref}\_i}\, p_{\mathrm{r}\_i}(f_{\mathrm{p}}, AFD)}{N_{\mathrm{b}\_i}} \tag{4}$$

2.2 Initiation model considering initial pore

Based on Murakami's assumption, the crack initiation phase is related to the maximum stress intensity factor $K_{\max}$ generated by near-surface pores [16]. Thus, high $K_{\max}$ values accelerate crack initiation, thereby reducing the initiation cycles N_{i} to the total life N_{t} ratio [10,12]. In addition, not only does $K_{\max}$ affect the initiation cycles ratio, but it also depends on the total cycle range of the evaluated case. For this reason, in the lower cycle domain inside the HCF regime, the N_i to N_{t} ratio is considerably lower than in the higher cycle domain [10]. Consequently, the initiation cycles N_{i} were estimated as a ratio of the total life N_{t} (5) by means of the function $\alpha(K_{\max}, N_b)$ dependent on the stress intensity factor $K_{\max}$ and cycle domain represented by the Basquin total life N_b of the evaluated case.

$$N_i = \alpha(K_{\max}, N_{\mathrm{b}})N_{\mathrm{t}} \tag{5}$$

To this end, firstly an analytical model to estimate stress intensity factor $K_{\max}$ depending on the initial pore characteristics was obtained. Then, the function $\alpha(K_{\max}, N_b)$ that determines the N_{i} cycles to total life N_{t} ratio was established.

2.2.1 Stress intensity factor model depending on the initial pore

To develop the stress intensity factor model, firstly the most relevant initial pore characteristics were identified. According to many authors [16,26], the key factors in the calculation of $K_{\max}$ are the distance to the surface d_{V} and the size of the pore φ. Besides these, some authors also reported the morphology of the pores as a relevant factor in the stress intensity factor calculation [27]. Therefore, a two-level numerical sensitivity analysis was performed considering the three main parameters reported in the literature. Moreover, horizontal distance to crack tip d_{H} and pore orientation considering morphology were also included. For the morphology sensitivity analysis, two real initial pores geometries in the fracture surface were selected; the first with a smooth pseudo-spherical shape and the second with an irregular dendritic shape. Table 2 shows the studied pore variables as well as the defined range of values. All different pore parameter values were specified from a LPDC component fractographic analysis data.

Table 2. Pore variables and ranges considered for the stress intensity factor model.

Factor	**Min value**	**Max value**
d_V (mm)	0.05	0.5
d_H (mm)	0	0.1
φ (mm)	0.1	0.3
Orientation angle	0º	90º
Morphology	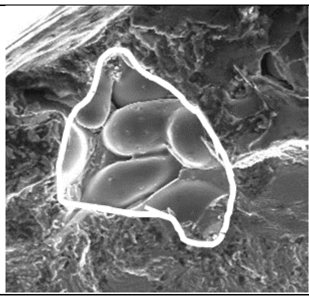	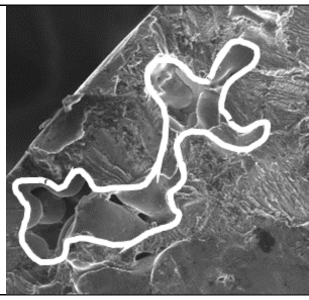

The simplified numerical sensitivity analysis was performed by means of a 5x2.5 mm^2 2D plane strain XFEM model where the real pore geometries, digitalized from the fractographic study were implemented as shown in Fig. 4. A global mesh size of 0.5 mm and a local mesh size of 0.005 mm near the pores were used. An initial crack of 0.5 mm length was defined in the centre of the top side of the model and the different pore geometries were located in the vertical and horizontal position as well as in angle with respect to it.

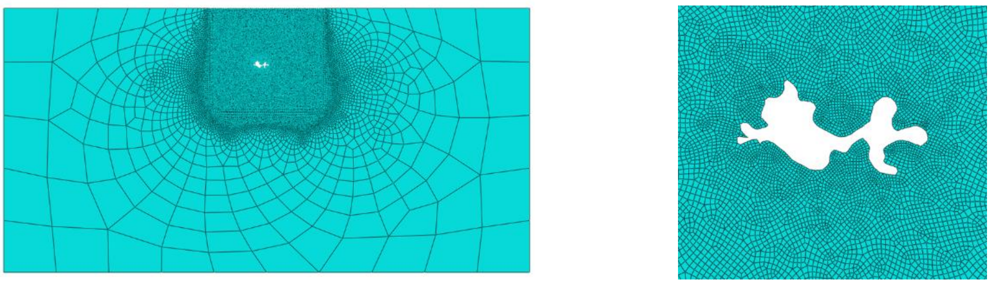

(a) (b)

Fig. 4. a) XFEM model used for the first DOE. b) Zoom of the mesh around the pore.

From the first analysis, the two most influential parameters, the Feret Diameter φ and the vertical distance to surface d_V, were identified. After this, a second analysis was performed in order to obtain the K_{max} response surface equation with respect to both parameters. Table 3 shows the studied conditions within the specified range.

Table 3. Values for dv*, and φ used in the second analysis to obtain the* K_{max} *response surface equation.*

Factor	Value 1	Value 2	Value 3	Value 4	Value 5	Value 6	Value 7
d_V (mm)	0.01	0.03	0.05	0.1	0.2	0.5	0.7
φ (mm)	0.1	0.3	0.5	1	-	-	-

2.2.2 *Initiation cycles to total ratio function*

The function $\alpha(K_{max}, N_b)$ that determines the N_i to total life N_t ratio is obtained by means of the following procedure:

1. **Estimation of each specimen's initiation number of cycles:** First, the initiation number of cycles of each tested specimen during the S-N curve characterisation was estimated. With this in mind, propagation cycles of each specimen were estimated based on the N_p estimation procedure presented in Section 2.1. Then, initiation cycles of each tested specimen were obtained as the difference between the experimental total life and the estimated propagation number of cycles (6)

$$N_i = N_{exp} - N_p \tag{6}$$

2. **Obtaining α value for each specimen:** Once the initiation number of cycles of each specimen had been estimated, the particular α value for each specimen was obtained (7)

$$\alpha = N_i / N_{exp} \tag{7}$$

3. **Obtaining K_{max} for each specimen:** Based on the fractographic study data, the K_{max} valued for each specimen was estimated considering the initial pore size φ and the distance to surface d_v based on the procedure presented in Section 2.2.1.

4. ***Obtaining the $\alpha(K_{max}, N_b)$* surface equation:** Finally, the α value for each specimen was represented with respect to the estimated K_{max} and N_b values; and the $\alpha(K_{max}, N_b)$ surface

equation was obtained by means of best fit technique. For a better performance of the best fit technique, two additional constraints were specified:

i. For K_{max} values above 650 MPa√mm, which corresponds to the specimens where the initial pore was located in the surface, the initiation phase was neglected and, consequently $\alpha=0$.

ii. Wang *et al.* [6] reported for an A356-T6 aluminium alloy that a pore with a size less than 25-50 µm did not produce propagation. Consequently, for pore sizes below 25 µm, which corresponds to a K_{max} lower than 385 MPa√mm, the α value was set to 1.

2.3 Total life estimation

Once the propagation number of cycles N_p and $\alpha(K_{max}, N_b)$ of the evaluated case can be estimated considering f_p, *AFD*, φ and d_v, the total life may be obtained as follows (8, 9, 10):

$$N_t = \alpha \cdot N_t + N_p \tag{8}$$

$$N_t(1-\alpha) = N_p \tag{9}$$

$$N_t = N_p / (1-\alpha) \tag{10}$$

3 EXPERIMENTAL PROCEDURE

3.1 S-N curve characterisation

The S-N curve characterisation of the A356-T6 Sr modified alloy solutionized at 540 ºC for 6 h and artificially aged at 155 ºC for 6 h was conducted with specimens of 6 mm diameter and 40 mm gauge length, according to ASTM-E466 standard, obtained from LPDC automotive knuckle arms. Fig. 5a) and b) respectively show the specimens' dimensions and the location in the knuckle arm from where they were obtained.

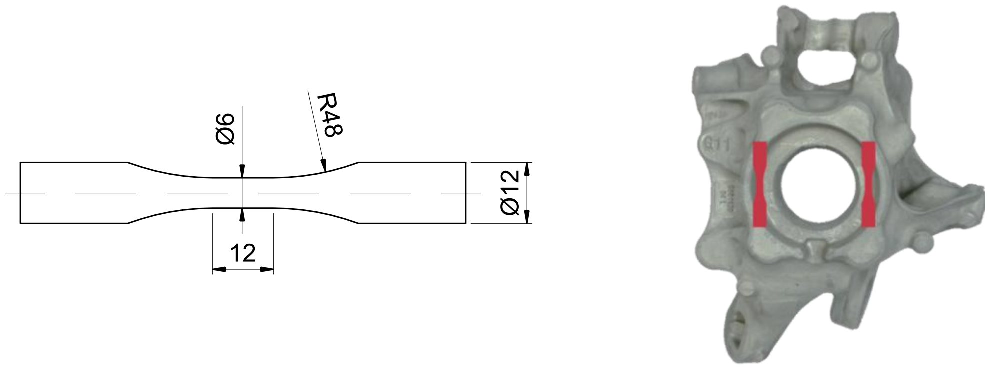

(a) (b)

Fig. 5. a) Fatigue specimens' dimensions and b) location in the LPDC knuckle arm from where they were obtained

The fatigue tests were performed at room temperature using an MTS 810 servo-hydraulic test machine equipped with a load cell of 100 kN at a stress ratio R=-1 and a frequency of 10 Hz according to ASTM-E466 standard. Four stress amplitudes were tested for characterization: 120, 110, 80 and 70 MPa. Run out was set to $5\cdot10^6$ cycles.

3.2 *Fractographic analysis*

After the tests, a fractographic analysis of all the specimens used in the S-N curve characterisation stage as well as the ones used in the procedure validation stage was performed to obtain the fractographic porosity f_p, Average Feret Diameter *AFD*, the Feret Diameter φ of the pore where the crack was initiated and the distance to surface d_v. To this end, fracture surface examination was carried out using an FEI Nova Nano SEM 450.

For each specimen, firstly, the contour boundaries of all the pores in the fractographic surface were marked and the total area of the pores was obtained according to the used scale factor by means of the Image J software [28]. Secondly, the fractographic porosity f_p was estimated as the ratio between the total area of the pores and the area of the fracture surface.

In addition, the pore size was represented by the Ferets Diameter, which is the longest distance between any two points along the region of interest boundary. For each pore, the corresponding

Feret Diameter was calculated by means of the Rotating Callipers technique. Then, the *AFD* value was determined as the mean value of all the measured Feret Diameters.

Finally, the initial pore was manually identified and the distance to the surface and the Feret Diameter values were obtained.

3.3 Experimental model validation tests

The proposed fatigue model was developed based on the S-N curve characterisation specimens' data. In order to validate the accuracy of the proposed model, additional fatigue tests were performed by following the same methodology as that explained in Section 3.1. Specimens were also obtained from LPDC knuckle arms at same locations. Validation tests were performed at R=-1 stress amplitudes of 110, 100, 85, and 75 MPa.

4 RESULTS AND DISCUSSION

4.1 Characterisation of LPDC A356-T6

4.1.1 S-N curve characterization

Fig. 6 shows the life of the specimens tested at the specified load levels as well as the fitted Basquin S–N curve (dotted line) with the following parameters: $\sigma_f{}'$ =1191.79 MPa and b= -0.1981. It can be observed that the scatter in life for the same load level increases for the higher domain in the HCF regime.

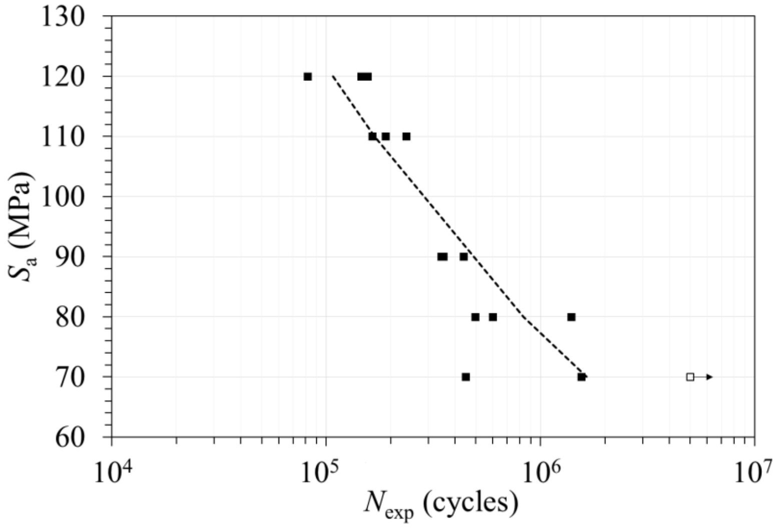

Fig. 6. S-N characterization curve. Empty symbols with arrows indicate run out specimens.

4.1.2 Fractographic analysis

Fig. 7. shows an example of a specimen fracture surface where the pores present in the surface and the crack initiation pore are highlighted.

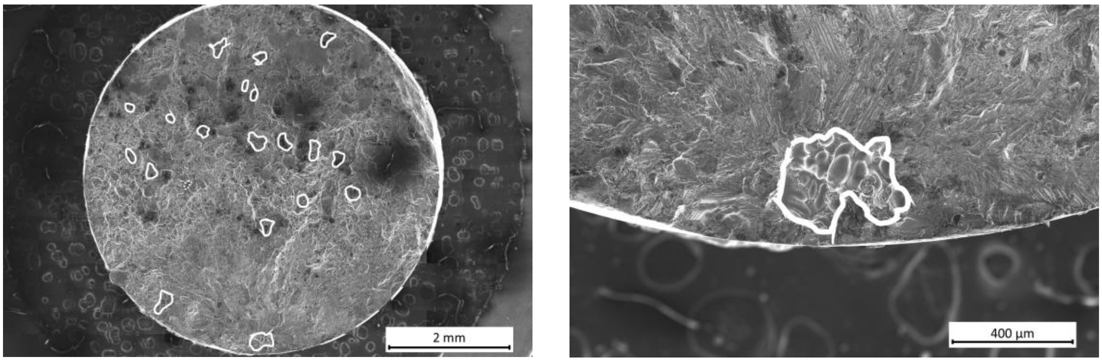

(a) (b)

Fig. 7. Representative fracture surface highlighting a) fractographic average porosity f_p and b) crack initiation pore.

The results of the fractographic inspection of the specimens used for the S-N curve characterisation are set out in Table 4. As can be observed, for each stress amplitude the fatigue life decreases with increasing f_p and φ.

Table 4. Results of porosity for the samples used in characterization.

Id.	**S_a (MPa)**	**N_{exp} (cycles)**	**Fractographic porosity**		**Crack initiation pore**	
			f_p%	***AFD* (mm)**	**φ (mm)**	**d_V (mm)**

C_120_1	120	155765	0.66	0.12	0.146	0
C_120_2	120	145470	1.7	0.16	0.344	0
C_120_3	120	81898	3.18	0.2	0.547	0
C_110_1	110	189654	0.95	0.12	0.249	0.015
C_110_2	110	164285	4.34	0.25	0.570	0
C_110_3	110	236106	0.51	0.13	0.127	0.012
C_90_1	90	344584	0.96	0.15	0.408	0
C_90_2	90	352414	2.92	0.15	0.440	0.040
C_90_3	90	437269	0.76	0.11	0.192	0.044
C_80_1	80	599318	1.23	0.10	0.193	0
C_80_2	80	1393739	0.64	0.14	0.148	0
C_80_3	80	495164	0.88	0.15	0.260	0
C_70_1	70	1550358	1.34	0.16	0.214	0
C_70_2	70	447473	3.29	0.24	0.86	0
C_70_3	70	Run Out	-	-	-	-

4.2 Propagation model

To obtain the propagation model, first reference specimens where the crack initiation pore was located in the surface, and consequently initiation cycles are negligible, were identified. Thus, the reference propagation speed ratio p_r=1 was established for the average measured values of f_p = 2.56 % and *AFD* = 0.20 mm. Fig. 8 a), b) and c) respectively show fractographic analysis examples of crack initiation pores (highlighted in the figure) located in the surface of specimens tested at stress amplitudes of 120, 90 and 70 MPa.

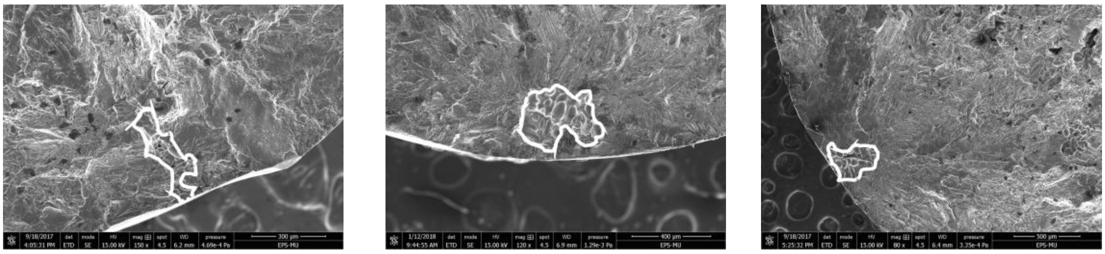

a) S_a=120MPa b) S_a=90MPa c) S_a 70MPa

Fig. 8. Examples of crack initiation pores located in the surface of specimens tested at a) 120MPa, b) 90MPa and c) 70MPa stress amplitudes

Next, the propagation speed ratio surface response $p_r(f_p,AFD)$ (11) within the specified f_p and *AFD* range (Table 1) was obtained from the XFEM sensitivity study and is represented in Fig. 9. It is observed that, as pointed out in the literature [12,19], the increase of both f_p and *AFD*, increase the propagation rate. However, it can be highlighted that, for the studied range, f_p is the most affecting parameter while *AFD* presents a lower effect. The obtained $p_r(f_p,AFD)$ equation (11) allows estimating the propagation speed ratio within the specified LPDC range according to the specific f_p and *AFD* values of the evaluated case.

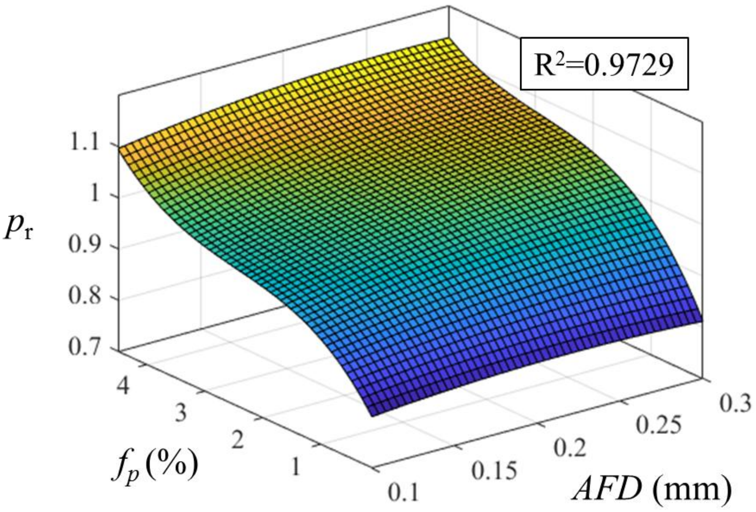

Fig. 9. $p_r(f_p,AFD)$ response surface.

$$p_r(f_p, AFD) = p_{00} + p_{10}AFD + p_{01}f_p + p_{20}AFD^2 + p_{11}AFD\cdot f_p + p_{02}f_p^{\,2} + p_{21}AFD^2\cdot f_p + p_{12}AFD\cdot f^2 + p_{03}f^3 \qquad (11)$$

Where:

p_{00}= 0.7438	p_{10}= 0.5253	p_{01}= 0.1436
p_{20}= -1.259	p_{11}= -0.3574	p_{02}= -0.05718
p_{21}= -0.06387	p_{12}= -0.06466	p_{03}= 0.008743

Once equation (11) had been obtained, the correction function $C(N_b)$ (12) was determined by applying the best fit technique to equation (4) results.

$$C(N_b) = -3.29\cdot 10^{-7}\cdot N_b + 0.8357 \qquad (12)$$

Finally, the propagation model for LPDC A356-T6 alloy (13) was assembled based on equations (2), (11) and (12)

$$N_p(f_p, AFD) = \left(\frac{S_a}{\sigma'_f}\right)^{\frac{1}{b}} \frac{-3.29 \cdot 10^{-7} \cdot N_b + 0.8357}{p_{00} + p_{10}AFD + p_{01}f_p + p_{20}AFD^2 + p_{11}AFD \cdot f_p + p_{02}f_p^2 + p_{21}AFD^2 \cdot f_p + p_{12}AFD \cdot f^2 + p_{03}f^3} \quad (13)$$

4.3 Initiation model

4.3.1 Two-level stress intensity factor sensitivity analysis

Fig. 10 represents the effect on K_{max} value of each variable used in the two-level sensitivity study. This effect has been calculated according to the methodology presented in [29]. It is observed that in accordance with the literature review [16,26], the most influencing features are d_V, φ and the interaction between them. Nevertheless, in contrast with [27,30]'s observations, and in accordance with other authors [16,31,32], the morphology of the pores did not have a remarkable influence within the studied range. Based on these results, a second detailed sensitivity study was carried out in order to obtain the $K_{max}(d_v, \varphi)$ surface response.

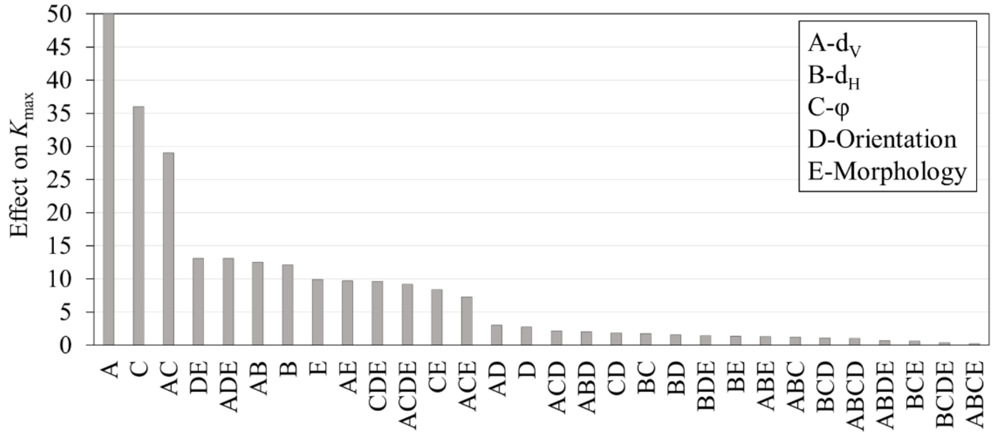

Fig. 10. Results of the two-level sensitivity study.

4.3.2 Stress intensity factor response surface

The $K_{max}(\varphi, d_V)$ response surface equation (14) was obtained from the detailed sensitivity study for the ranges of φ and d_V included in Table 3 and is graphically represented in Fig. 11. Thus, the stress intensity factor based on the initial pore size and distance to the surface of the evaluated case can be estimated within the specified range. It is observed that the pore size becomes especially relevant when the distance to the surface of the pore is short. For higher distances to surface, the pore size does not especially affect the K_{max} value, which is in accordance with the findings of Siddique et al. [33].

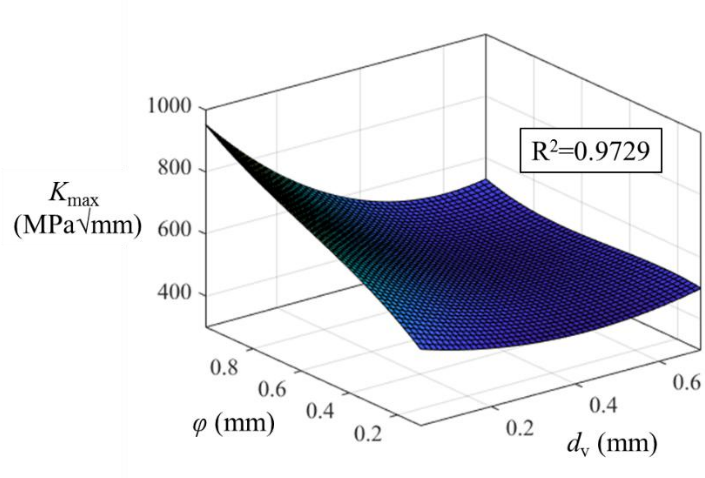

Fig. 11. $K_{max}(\varphi, d_V)$ *response surface*

$$K_{max}(d_v,\varphi)=k_{00}+k_{10}d_v+k_{01}\varphi+k_{20}d_v^{\,2}+k_{11}d_v\cdot\varphi+k_{02}\varphi^2+k_{21}d_v^{\,2}\cdot\varphi+ \\ +k_{12}d_v\cdot\varphi^2+k_{03}\varphi^3 \tag{14}$$

Where:

k_{00}= 506.4	k_{10}= -216.9	k_{01}= 664.7
k_{20}= 217.6	k_{11}= -1442	k_{02}= -459.1
k_{21}= 1158	k_{12}= 17.84	k_{03}= 308.4

4.3.3 Initiation cycles to total ratio function

Fig. 12 shows the initiation cycles to total ratio function $\alpha(K_{max},N_b)$ (15) for LPDC A356-T6 aluminium alloy, assembled following the methodology explained in Section 2.2.2. It is observed that the initiation phase, related to α values, is more relevant in the higher domain of the HCF regime. In addition, for a specific domain inside the HCF regime, the increase of K_{max} values decreases the α values and, consequently, the number of cycles required for crack initiation, which is in agreement with the literature [10]. For high K_{max} values, which are related to big pore sizes φ and low distances to surface d_v (see Fig. 11), α values tend to zero, which means that the crack initiation cycles are negligible.

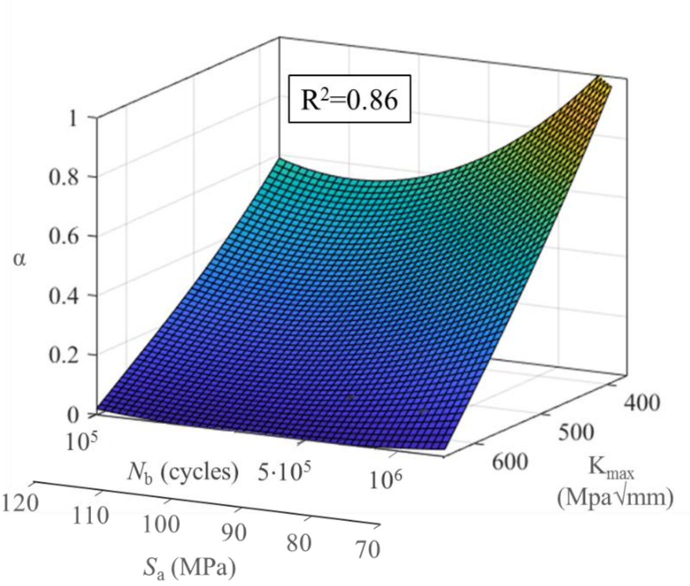

Fig. 12. Surface that relates α, K_{max} and N_b.

$$\alpha(K_{max}, N_b) = a_{n\_00} + a_{n\_10}K_{max} + a_{n\_01}N_b + a_{n\_20}K_{max}^2 + a_{n\_11}K_{max} \cdot N_b + a_{n\_02}N_b^2 + a_{n\_21}K_{max}^2 \cdot N_b + a_{n\_12}N_b \cdot K_{max}^2 + a_{n\_03}N_b^3 \quad (15)$$

Where:

a_{n_00}= 1.467	a_{n_10}= 8.107·10^{-7}	a_{n_01}= -0.002779
a_{n_20}= 7.371·10^{-14}	a_{n_11}= -1.689·10^{-9}	a_{n_02}= 5.495·10^{-7}
a_{n_21}= -1.372·10^{-16}	a_{n_12}= 7.033·10^{-13}	a_{n_03}= 3.808·10^{-10}

However, in order to estimate the fatigue life for a certain load stress amplitude, equation (15) was rewritten as $\alpha(K_{max}, S_a)$ (16), dependent on S_a, by combining with the Basquin equation (1).

$$\alpha(K_{max}, S_a) = a_{s\_00} + a_{s\_10}K_{max} + a_{s\_01}S_a + a_{s\_20}K_{max}^2 + a_{s\_11}K_{max} \cdot S_a + a_{s\_02}S_a^2 + a_{s\_21}K_{max}^2 \cdot S_a + a_{s\_12}S_a \cdot K_{max}^2 + a_{s\_03}S_a^3 \quad (16)$$

Where:

a_{s_00}= 14.07	a_{s_10}= -0.1966	a_{s_01}= -0.02992
a_{s_20}= 8.569·10^{-4}	a_{s_11}= 3.151·10^{-4}	a_{s_02}= 1.917·10^{-5}
a_{s_21}= -1.267·10^{-6}	a_{s_12}= -3.448·10^{-8}	a_{s_03}= -8.848·10^{-9}

4.4 *Porosity based life prediction model for LPDC A356-T6*

Finally, the porosity based life prediction analytical model for LPDC A356-T6 aluminium alloy (17) was obtained by considering $N_p(f_p, AFD)$ equation (13), and $\alpha(K_{max}, S_a)$ function (16).

$$N_t = \frac{\left(\frac{S_a}{\sigma'_f}\right)^{\frac{1}{b}\frac{-3.29\cdot 10^{-7}\cdot N_b + 0.8357}{p_{00}+p_{10}AFD+p_{01}f_p+p_{20}AFD^2+p_{11}AFD\cdot f_p+p_{02}f_p^{\ 2}+p_{21}AFD^2\cdot f_p+p_{12}AFD\cdot f^2+p_{03}f^3}}}{1-(a_{s\_00}+a_{s\_10}K_{max}+a_{s\_01}S_a+a_{s\_20}K_{max}^{\ 2}+a_{s\_11}K_{max}\cdot S_a+a_{s\_02}S_a^{\ 2}+a_{s\_21}K_{max}^{\ 2}\cdot S_a++a_{s\_12}S_a\cdot K_{max}^{\ 2}+a_{s\_03}S_a^{\ 3})} \quad (17)$$

4.5 *Validation*

The porosity based life prediction model for LPDC A356-T6 was validated with additional fatigue tests at 110, 100, 85 and 75 MPa stress amplitude loads. Fig. 13 shows the experimental life results for the tested cases.

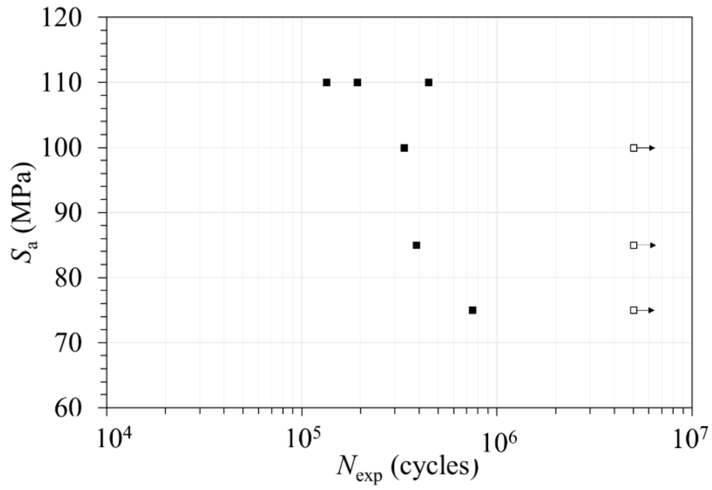

Fig. 13. S-N curve for validation tests. Empty symbols with arrows indicate run out specimens.

4.5.1 *Fractographic analysis*

Table 5 shows each validation test life as well as the f_p, *AFD,* φ and d_v parameters measured during the fractographic analysis. In the case of Run Out tests, those parameters could not be measured as the rupture of the specimens did not occur.

Table 5. f_p, *AFD,* φ, d_v *values for validation samples.*

Id.	S_a (MPa)	N_{exp} cycles	Fractographic porosity		Initial pore	
			f_p (%)	*AFD* (mm)	φ (mm)	d_V (mm)
V_110_1	110	446564	0.76	0.13	0.058	0.065
V_110_2	110	192410	0.83	0.12	0.414	0.044
V_110_3	110	133879	2.08	0.4	0.312	0
V_100_1	100	334254	0.48	0.12	0.146	0
V_100_2	100	RO	-	-	-	-
V_85_1	85	387002	0.99	0.11	0.529	0
V_85_2	85	RO	-	-	-	-
V_75_1	75	748150	0.72	0.1	0.205	0.046
V_75_2	75	RO	-	-	-	-

4.5.2 Model validation

The validation of the model was performed in two stages. Firstly, the validity of the model to estimate the fatigue life of the specimens used in the S-N curve characterisation was evaluated (Table 6). Secondly, the validity of the model to estimate the fatigue life of additional fatigue tests, whose data was not used to build the model, was evaluated (Table 7).

Fig. 12 represents experimental life (solid colour) of both characterisation (Fig. 12.a) and validation samples (Fig. 12.b), together with life estimations obtained with the porosity model for each case (empty symbols). It is noteworthy that, for each tested load amplitude, the proposed model predicts in every case the specimens that present higher and lower life, while conventional fatigue models provide a single life prediction for each tested load case. In addition, the Basquin regression of both, experimental and predicted cases, are compared. It is observed that the deviation between both curves is negligible, which indicates that the overall prediction trend of the proposed model is in accordance with the experimental behaviour.

Table 6. Experimental life vs. theoretical life of the S-N characterisation specimens.

Id.	S_a (MPa)	N_{exp} (cycles)	N_b (cycles)	N_p (cycles)	K_{max} (MPa √mm)	α	N_t (cycles)	*Log error (%)*	*Abs error (%)*
C_120_1	120	155765	107871	97917	474	0.34	146334	0.52	6.1
C_120_2	120	145470	107871	91218	615	0.08	96823	3.42	33.4
C_120_3	120	81898	107871	83195	761	0	82135	0.03	0.3
C_110_1	110	189654	167364	145754	547	0.17	172604	0.78	9.0
C_110_2	110	164285	167364	116224	777	0	116163	2.89	29.3
C_110_3	110	236106	167364	148960	420	0.41	251239	0.50	6.4
C_90_1	90	344584	460884	346327	661	0	340539	0.09	1.2
C_90_2	90	352414	460884	312606	649	0	308609	1.04	12.4
C_90_3	90	437269	460884	355067	454	0.43	613497	2.61	40.3
C_80_1	80	599318	835232	892415	525	0.35	766008	1.84	27.8
C_80_2	80	1393739	835232	911283	428	0.65	1472485	0.39	5.6
C_80_3	80	495164	835232	905075	555	0.27	686506	2.49	38.6
C_70_1	70	1550358	1638883	1695154	514	0.53	1018211	2.95	34.3
C_70_2	70	447473	1638883	1471001	428	0	449074	0.03	0.4

C_70_3	70	Run Out	1638883	-	-		146334	-	-

Table 7. Experimental life vs. theoretical life of validation specimens.

Id.	S_a **(MPa)**	N_{exp} **(cycles)**	N_b **(cycles)**	N_p **(cycles)**	K_{max} **(MPa √mm)**	α	N_t **(cycles)**	***Log error (%)***	***Abs error (%)***
V_110_1	110	446564	167364	182006	343	0.63	390259	1.04	12.6
V_110_2	110	192410	167364	145061	619	0.05	151328	1.97	21.4
V_110_3	110	133879	167364	142841	592.9	0.09	135747	0.12	1.4
V_100_1	100	334254	270776	283856	474	0.31	331990	0.05	0.7
V_100_2	100	RO	-	-	-	-	-	-	-
V_85_1	85	387002	615035	664276	748	0	426426	0.75	10.2
V_85_2	85	RO	-	-	-	-	-	-	-
V_75_1	75	748150	1156898	579391	371	0.5	944406	1.72	26.2
V_75_2	75	RO	-	-	-	-	-	-	-

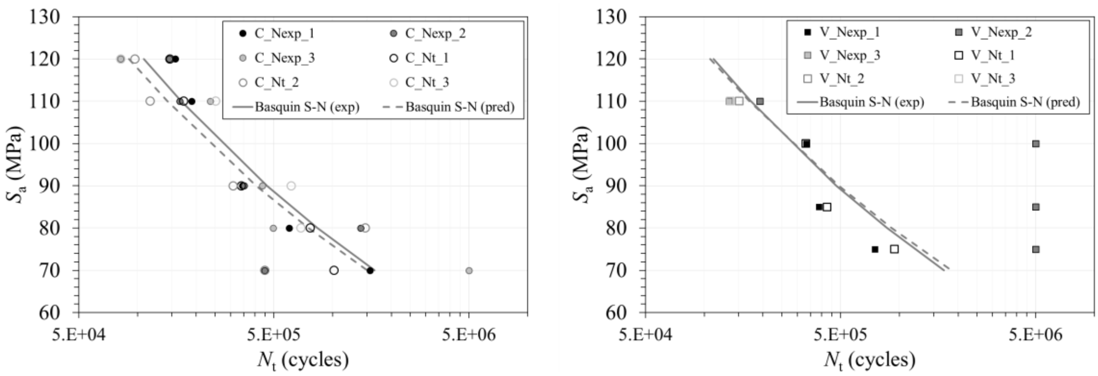

(a) (b)

Fig. 14. Life predictions using the proposed model for a) Characterization samples and b) Validation samples.

Fig. 15 presents the life prediction logarithmic error of both the proposed model and Basquin model. It is observed that the quantitative life prediction of the proposed model presents in most cases a logarithmic error below 2 % and an absolute error below 16%. However, in some cases the quantitative life prediction presents logarithmic errors up to 3 % (40% absolute error) which indicates that, even though the porosity is the main affecting parameter, there are other affecting variables not considered in the model. Fig. 16 shows an example of the fractographic surfaces of samples C_110_1 and C_80_3. In the first, a high amount of inclusions was found while, in the second, a big pore near the initiation pore that could accelerate initiation was observed.

Nevertheless, the maximum logarithmic error in life prediction of 3.4% (33.4% absolute error) obtained with the proposed model is still below the maximum logarithmic error of 10% (266% absolute error) that the Basquin model presents.

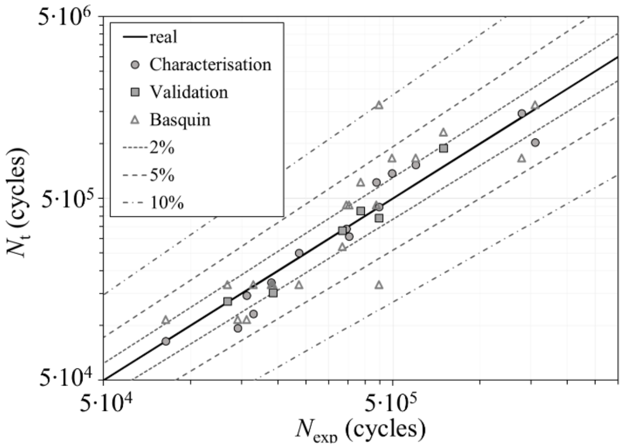

Fig. 15. Comparison of predicted to real cycle error of the proposed porosity model and the Basquin model.

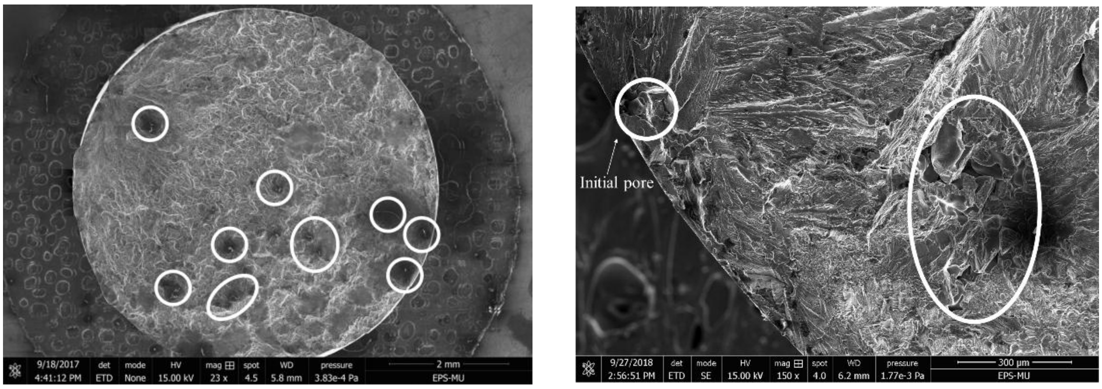

(a)

(b)

Fig. 16. Detailed fracture surfaces in specimens a) C_100_1 and b) C_80_3

5 CONCLUSIONS

The scatter presented in samples tested at the same loads characterizes the HCF regime. Although there are many sources that generate this variability in fatigue behaviour, porosity is one of the main affecting parameters in the fatigue scatter of casting components. Therefore, in the present work an alternative fatigue assessment procedure, which accounts for the effect of porosity on the initiation and propagation phases, was developed and implemented for LPDC A356-T6 aluminium alloy.

Results have shown that, by considering the effect of porosity on both initiation and propagation phases, it is possible to predict qualitatively the scatter trend of each sample tested in all cases studied. Moreover, quantitative life prediction presents an average logarithmic error below 2% and an absolute average error below 16% in life prediction. Nevertheless, porosity is not the only affecting parameter in fatigue life scatter. Thus, quantitative logarithmic deviations up to 3.4 % and absolute deviations up to 40 % were found in some cases. Fractographic analysis showed that, for example, inclusion levels higher or lower than the average of the specimens tested to build the model, or the existence of big pores in the subsurface near the initiation pore, can directly affect the fatigue life prediction.

The main drawback of the presented fatigue assessment model is that the required porosity parameters, f_p, *AFD*, φ and d_v, are difficult to measure before the rupture of the tested sample as those parameters are typically measured from the fracture surface (DT). Thus, in order to use the proposed procedure as a predictive tool in the design process of casting parts, it is necessary to have an extensive statistical database of the typical f_p, *AFD*, φ and d_v values of tested components that represent the process window. Therefore, the proposed model is appropriate for the auto parts manufacturing industry where high series of different components in the same material are produced. Thus, once the process window has been characterised, the acceptance limits of f_p, *AFD*, φ and d_v can be defined. These limit values can be implemented in the proposed model during the design process, thereby ensuring the fatigue performance of accepted components.

Alternatively, NDT methods, such as computed tomography, could allow measuring porosity characteristics of an evaluated component before testing. From the digitalised 3D porosity data, the most probable fracture surface could be identified by considering the loading conditions. Thus, the proposed model could be fed with the digital measurements of the required porosity parameters in order to predict fatigue life in components.

Acknowledgements

The authors would like to thank FAGOR Ederlan Group for support in the development of the present work. Furthermore, the authors would like to acknowledge the financial support provided by the Ministry of Industry Economics and Competitiveness of the Spanish Government by means of ALPRE project (RTC-2015-3822-4) and the FEDER funds from the European Union.

References

[1] Stephens R., Fatemi A, Stephens RR, Fuchs H. Metal fatigue in engineering 2001.

[2] Yi JZ, Gao YX, Lee PD, Flower HM, Lindley TC. Scatter in fatigue life due to effects of porosity in cast A356-T6 aluminum-silicon alloys. Metall Mater Trans A 2003;34:1879–90. doi:10.1007/s11661-003-0153-6.

[3] Bonollo F, Urban J, Bonatto B, Botter M. Gravity and low pressure die casting of aluminium alloys: a technical and economical benchmark. La Metall Ital 2005:23–32.

[4] Iben Houria M, Nadot Y, Fathallah R, Roy M, Maijer DM. Influence of casting defect and SDAS on the multiaxial fatigue behaviour of A356-T6 alloy including mean stress effect. Int J Fatigue 2015;80:90–102. doi:10.1016/j.ijfatigue.2015.05.012.

[5] Roy MJ, Nadot Y, Nadot-Martin C, Bardin PG, Maijer DM. Multiaxial Kitagawa analysis of A356-T6. Int J Fatigue 2011;33:823–32. doi:10.1016/j.ijfatigue.2010.12.011.

[6] Wang QG, Apelian D, Lados D a. Fatigue behavior of A356-T6 aluminum cast alloys. Part I. Effect of casting defects. J Light Met 2001;1:73–84. doi:10.1016/S1471-5317(00)00008-0.

[7] Lee C Do, Yoo SJ. Dependence of Fatigue Life of Low-Pressure Die-Cast A356 Aluminum Alloy on Microporosity Variation. Met Mater Int 2014;20:601–12. doi:10.1007/s12540-014-4004-3.

[8] Zheng X, Cui H, Engler-Pinto CC, Su X, Wen W. Statistical relationship between fatigue crack initiator size and fatigue life for a cast aluminum alloy. Mater Sci Eng A 2013;580:71–6. doi:10.1016/j.msea.2013.05.045.

[9] Le VD, Morel F, Bellett D, Saintier N, Osmond P. Multiaxial high cycle fatigue damage mechanisms associated with the different microstructural heterogeneities of cast aluminium alloys. Mater Sci Eng A 2016;649:426–40. doi:10.1016/j.msea.2015.10.026.

[10] Ammar HR, Samuel AM, Samuel FH. Porosity and the fatigue behavior of hypoeutectic and hypereutectic aluminum–silicon casting alloys. Int J Fatigue 2008;30:1024–35. doi:10.1016/j.ijfatigue.2007.08.012.

[11] Avalle M, Belingardi G, Cavatorta MP, Doglione R. Casting defects and fatigue strength of a die cast aluminium alloy: A comparison between standard specimens and production components. Int J Fatigue 2002;24:1–9. doi:10.1016/S0142-1123(01)00112-8.

[12] Ammar HR, Samuel AM, Samuel FH. Effect of casting imperfections on the fatigue life of 319-F and A356-T6 Al–Si casting alloys. Mater Sci Eng A 2008;473:65–75. doi:10.1016/j.msea.2007.03.112.

[13] González R, González A, Talamantes-Silva J, Valtierra S, Mercado-Solís RD, Garza-Montes-De-Oca NF, et al. Fatigue of an aluminium cast alloy used in the manufacture of automotive engine blocks. Int J Fatigue 2013;54:118–26. doi:10.1016/j.ijfatigue.2013.03.018.

[14] Li B, Shen Y, Hu W. Casting defects induced fatigue damage in aircraft frames of ZL205A aluminum alloy - A failure analysis. Mater Des 2011;32:2570–82. doi:10.1016/j.matdes.2011.01.039.

[15] Le V-D, Morel F, Bellett D, Pessard E, Saintier N, Osmond P. Microstructural-based Analysis and Modelling of the Fatigue Behaviour of Cast Al-Si Alloys. Procedia Eng 2015;133:562–75. doi:10.1016/j.proeng.2015.12.630.

[16] Murakami Y. Material defects as the basis of fatigue design. Int J Fatigue 2012;41:2–10. doi:10.1016/j.ijfatigue.2011.12.001.

[17] Susmel L, Taylor D. On the use of the Theory of Critical Distances to predict static failures in ductile metallic materials containing different geometrical features. Eng Fract Mech 2008;75:4410–21. doi:10.1016/j.engfracmech.2008.04.018.

[18] Nadot Y, Billaudeau T. Multiaxial fatigue limit criterion for defective materials. Eng Fract Mech 2006;73:112–33. doi:10.1016/j.engfracmech.2005.06.005.

[19] Tenkamp J, Koch A, Knorre S, Krupp U, Michels W, Walther F. Defect-correlated fatigue assessment of A356-T6 aluminum cast alloy using computed tomography based Kitagawa-Takahashi diagrams. Int J Fatigue 2018;108:25–34. doi:10.1016/j.ijfatigue.2017.11.003.

[20] Linder J, Axelsson M, Nilsson H. The influence of porosity on the fatigue life for sand and permanent mould cast aluminium. Int J Fatigue 2006;28:1752–8. doi:10.1016/j.ijfatigue.2006.01.001.

[21] Leitner M, Garb C, Remes H, Stoschka M. Microporosity and statistical size effect on the fatigue strength of cast aluminium alloys EN AC-45500 and 46200. Mater Sci Eng A 2017;707:567–75. doi:10.1016/j.msea.2017.09.023.

[22] Fernández-Canteli A, Castillo E, López-Aenlle M, Seitl S. Using statistical compatibility to derive advanced probabilistic fatigue models. Procedia Eng 2010;2:1131–40. doi:10.1016/j.proeng.2010.03.122.

[23] Spangenberger AG, Lados DA, Coleman M, Birosca S, Hardy MC. Microstructural mechanisms and advanced characterization of long and small fatigue crack growth in cast A356-T61 aluminum alloys. Int J Fatigue 2017;97:202–13. doi:10.1016/j.ijfatigue.2016.12.029.

[24] Llavori I, Zabala A, Urchegui MA, Tato W, Gómez X. A coupled crack initiation and propagation numerical procedure for combined fretting wear and fretting fatigue lifetime assessment. Theor Appl Fract Mech 2019. doi:10.1016/j.tafmec.2019.03.005.

[25] Giner E, Sukumar N, Tarancón JE, Fuenmayor FJ. An Abaqus implementation of the extended finite element method. Eng Fract Mech 2009;76:347–68. doi:10.1016/j.engfracmech.2008.10.015.

[26] Ueno A, Miyakawa S, Yamada K, Sugiyama T. Fatigue behavior of die casting aluminum alloys in air and vacuum. Procedia Eng 2010;2:1937–43. doi:10.1016/j.proeng.2010.03.208.

[27] Tijani Y, Heinrietz A, Bruder T, Hanselka H. Quantitative evaluation of fatigue life of cast aluminum alloys by non-destructive testing and parameter model. Int J Fatigue 2013;57:73–8. doi:10.1016/j.ijfatigue.2013.05.017.

[28] https://imagej.nih.gov/ij/ n.d.

[29] Unzueta-Aranguren G, Orue-Irasuegi A, Esnaola-Arruti A, Eguren-Egiguren J. DESIGN OF EXPERIMENTS METHODOLOGY. CASE STUDY, LAUNCHER. DYNA 2019;94:16–21. doi:http://dx.doi.org/10.6036/8687.

[30] Maurel V, Dezecot S, Koster A, Buffiere J-Y, Szmytka F. 3D characterization and modeling of low cycle fatigue damage mechanisms at high temperature in a cast aluminum alloy. Acta Mater 2016;123:24–34. doi:10.1016/j.actamat.2016.10.028.

[31] Rotella A, Nadot Y, Piellard M, Augustin R, Fleuriot M. Fatigue limit of a cast Al-Si-Mg alloy (A357-T6) with natural casting shrinkages using ASTM standard X-ray inspection. Int J Fatigue 2018;114:177–88. doi:10.1016/j.ijfatigue.2018.05.026.

[32] Wang QG, Davidson CJ, Griffiths JR, Crepeau PN. Oxide Films, Pores and the Fatigue Lives of Cast Aluminum Alloys. Metall Mater Trans B 2006;37B:889–95.

[33] Siddique S, Imran M, Rauer M, Kaloudis M, Wycisk E, Emmelmann C, et al. Computed tomography for characterization of fatigue performance of selective laser melted parts.

Mater Des 2015;83:661–9. doi:10.1016/j.matdes.2015.06.063.